Electronic spin transport in graphene field-effect transistors

Popinciuc, M.; Jozsa, C.; Zomer, P. J.; Tombros, N.; Veligura, A.; Jonkman, H. T.; van Wees, B. J.

Published in:
Physical Review. B: Condensed Matter and Materials Physics

DOI:
10.1103/PhysRevB.80.214427

Publication date:
2009

Electronic spin transport in graphene field-effect transistors

M. Popinciuc,[1,*] C. Józsa,[2] P. J. Zomer,[2] N. Tombros,[2] A. Veligura,[2] H. T. Jonkman,[1] and B. J. van Wees[2]
[1]*Molecular Electronics, Zernike Institute for Advanced Materials, University of Groningen, Groningen, The Netherlands*
[2]*Physics of Nanodevices, Zernike Institute for Advanced Materials, University of Groningen, Groningen, The Netherlands*
(Received 6 August 2009; revised manuscript received 22 November 2009; published 30 December 2009)

Spin transport experiments in graphene, a single layer of carbon atoms ordered in a honeycomb lattice, indicate spin-relaxation times that are significantly shorter than the theoretical predictions. We investigate experimentally whether these short spin-relaxation times are due to extrinsic factors, such as spin relaxation caused by low impedance contacts, enhanced spin-flip processes at the device edges, or the presence of an aluminum oxide layer on top of graphene in some samples. Lateral spin valve devices using a field-effect transistor geometry allowed for the investigation of the spin relaxation as a function of the charge density, going continuously from metallic hole to electron conduction (charge densities of $n \sim 10^{12}$ cm^{-2}) via the Dirac charge neutrality point ($n \sim 0$). The results are quantitatively described by a one-dimensional spin-diffusion model where the spin relaxation via the contacts is taken into account. Spin valve experiments for various injector-detector separations and spin precession experiments reveal that the longitudinal (T_1) and the transversal (T_2) relaxation times are similar. The anisotropy of the spin-relaxation times $\tau_{\parallel}$ and $\tau_{\perp}$, when the spins are injected parallel or perpendicular to the graphene plane, indicates that the effective spin-orbit fields do not lie exclusively in the two-dimensional graphene plane. Furthermore, the proportionality between the spin-relaxation time and the momentum-relaxation time indicates that the spin-relaxation mechanism is of the Elliott-Yafet type. For carrier mobilities of $2 \times 10^3 - 5 \times 10^3$ cm^2/V s and for graphene flakes of $0.1-2$ μm in width, we found spin-relaxation times on the order of 50–200 ps, times which appear not to be determined by the extrinsic factors mentioned above.

DOI: 10.1103/PhysRevB.80.214427 PACS number(s): 72.25.−b

I. INTRODUCTION

Spintronics is the field of electronics that uses the spin of the charge carrier for the transport and manipulation of information. Preserving a spin state is fundamentally limited by the spin-orbit interaction which provides the mechanism(s) for spin relaxation. Carbon-based material systems promise a weak spin-orbit interaction (i.e., long spin-relaxation times) due to the low atomic number of carbon. Spin transport investigations have been reported for molecular systems and carbon nanotubes, see Ref. 1 for a review, and more recently for single or multilayer graphene.[2–14] The low dimensionality, the ability to control the charge-carrier type, and the density combined with the highest room-temperature carrier mobility reported so far for any material[15–17] make graphene a promising candidate for electronic applications. Especially relevant for spintronics are the high carrier mobilities and the possibly long spin-relaxation times which determine large spin-relaxation lengths, i.e., long distances over which the spin information can be transported and manipulated.

In previous experiments we deduced spin-relaxation times of 150 ps (spin-relaxation lengths of $1.5-2$ μm) at room temperature,[3] values confirmed by more recent findings.[12,14] These relaxation times are shorter than expected by at least one order of magnitude, pointing to an extrinsic spin-relaxation mechanism rather than to an intrinsic one. In this study, we present all electrical spin valve and spin precession experiments aiming at determining the possible causes for such short spin-relaxation times. From the experimental point of view, three major aspects are identified as discussed below. For theoretical investigations of the possible spin-relaxation mechanisms we refer to Refs. 18–25.

First, in the diffusive transport regime, electrical spin injection in high resistance materials from ferromagnetic metals with spin polarizations of less than 100% is highly inefficient due to the conductivity mismatch problem.[26] The spin accumulation created at the clean ferromagnetic metal/high-resistance material interface by the injection current prefers to flow back into the low impedance injector (where the spin orientation is readily lost due to strong spin-orbit coupling) rather than diffusing into the high impedance material. In order to realize efficient electrical spin injection and detection in graphene, a thin aluminum oxide layer has been introduced in between the ferromagnetic Co injector and detector, and graphene.[26–31] By providing a high contact resistance, the role of the aluminum oxide layer is to limit the back diffusion of spins into the injector and to realize a weakly coupled spin detector. Yet, in some experiments the contact resistances are comparable in magnitude with the graphene square resistance over one spin-relaxation length and significant spin relaxation occurs via the contacts. We quantify this effect by using a one-dimensional spin-diffusion model. Second, in all our previous experiments the whole graphene layer was covered by the thin aluminum oxide layer, a procedure which simplified the fabrication process. Whether this oxide layer, which needs to be only underneath the Co electrodes, induces extra spin relaxation was not known. In order to investigate this issue we performed experiments where the aluminum oxide barriers were present only underneath the Co electrodes. The third aspect is whether the low spin-relaxation times are due to spin scattering at the edges of the graphene flakes. Therefore, we performed spin transport experiments using narrow struc-

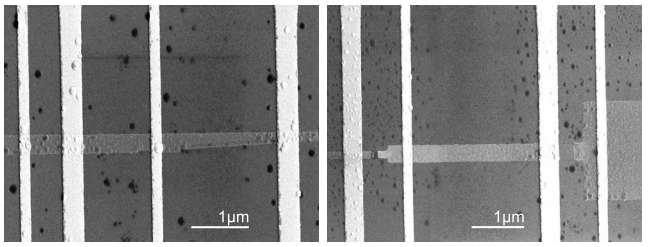

FIG. 1. SEM images of two graphene spin valves (type III devices, fabricated by etching). The graphene flakes (horizontal light gray areas) are contacted by four Co electrodes of different widths (vertical light areas).

tures (down to 100 nm in width, which is 15–20 times narrower than the spin-relaxation length).

This paper is organized as follows. In Sec. II we present experimental details (fabrication and measurement) followed by general electrical characteristics of the devices. In Sec. III we discuss modeling and experiments pertaining to the spin valve and spin precession experiments. After a short introduction regarding the functioning of a four-terminal spin valve device (Sec. III A) we discuss the influence of the contact resistance on the spin valve measurements (Sec. III B). We present spin valve experiments and discuss the length dependence of the spin signal in Secs. III C and III D. In Sec. III E we model the contact effects in spin precession experiments. Next, in Secs. III F and III G, we present experimental data and analysis regarding the issues raised in the previous paragraph. The gate voltage dependence of the spin transport which allows us to identify the spin-relaxation mechanism in our devices is discussed in Sec. III H. The paper ends with the conclusions section. Details of the modeling of spin relaxation via the contacts are presented in the Appendix.

II. DEVICE FABRICATION AND ELECTRICAL CHARACTERISTICS

In this study we compare the spin transport properties of three types of devices. Type I devices are based on naturally occurring graphene flakes (deposited using the scotch tape technique with widths of 300 nm or more) and contain the aluminum oxide layer all over graphene. Type II devices (also naturally occurring flakes) contain the aluminum oxide layer only underneath the Co electrodes. The comparison between the two types of devices enabled us to investigate whether the aluminum oxide layer present all over graphene introduces extra spin scattering. The type III devices were fabricated in order to establish if enhanced spin scattering processes occur at the device edges. These devices were fabricated by etching (device widths down to 100 nm) and contain aluminum oxide only underneath the Co electrodes. In Fig. 1 we show scanning electron micrographs (SEM) of two type III devices contacted by four ferromagnetic Co electrodes. In this section we present in detail the fabrication procedure and the measurement conditions followed by a short discussion of the general device electrical characteristics.

All devices were fabricated on a dry oxidized highly doped ($\rho=1$ mΩ cm) silicon substrate commercially available. The oxide was 500 or 300 nm thick. The application of a back gate voltage allows for the control of the charge-carrier type and density in the graphene flakes. The gate electrode was fabricated by etching the back side oxide of the wafer followed by the deposition of a 100-nm-thick Ti/Au layer. On this substrate we defined a set of Ti/Au markers using electron-beam lithography (EBL). Next, the substrate was cleaned by oxygen plasma in order to remove the polymeric residuals from the EBL step. Then, highly oriented pyrolytic graphite (from GE Advanced Ceramics and SPI) was cleaved with a scotch tape and firmly pressed against the substrate. The tape is peeled off the substrate leaving a random distribution of graphite pieces among which there are also single layer graphene flakes. Using an optical microscope, the flakes displaying the lowest contrast were selected as potential single layer candidates. After that, the single layers were identified by atomic force microscope (AFM) measurements using high cantilever amplitudes.[32] Since water or other molecules may be absorbed locally on graphene or the substrate, only flakes of thicknesses of $\leqslant 0.5$ nm were selected as single layer graphene. In a few cases Raman spectroscopy and quantum Hall effect experiments have been used to confirm our selection criteria.[32] Using the AFM pictures, the position of the flakes with respect to the known position of the Ti/Au markers is noted. Later on, this allowed for a precise positioning of the ferromagnetic electrodes. The fabrication procedure continued differently for the different types of devices as explained below.

For the type I samples, we continued with the thermal evaporation of a thin layer of Al (6 Å) in an ultrahigh vacuum (UHV) system with the substrate being liquid-nitrogen cooled. After that, the Al layer was oxidized for a minimum of 30 min in the load lock of the system in an oxygen atmosphere of about 100 mbar. Next, ferromagnetic electrodes of different widths were defined using EBL followed by electron-beam evaporation of Co in a high vacuum system. After lift-off in hot acetone for typically 10 min, the sample was glued on a chip carrier and electrical connections between the sample and the chip carrier were made using ultrasonic wire bonding. The sample was then placed in a vacuum container and measured. For the type I devices, the graphene flakes are completely covered by the thin aluminum oxide. In Figs. 2(a) and 2(b) we show AFM measurements of a graphene flake after the aluminum deposition. In spite of the cryogenic evaporation of Al, the oxide layer on graphene is granular in nature. SEM images, not shown here, support this observation. Roughness analysis of the aluminum oxide layer on several samples reveal root-mean-square values of 0.5–0.7 nm on graphene and about 0.3 nm on the SiO_2 substrate.

For the type II devices, the AlO_x layer was deposited only underneath the Co electrodes. After the flake deposition and identification, an EBL step was performed followed by the sequential deposition and oxidation of Al and the thermal evaporation of Co in the same UHV system. Due to the configuration of the UHV system the Al deposition on the cooled stage was done under an angle of 30° with respect to the sample normal. The deposition was set to take place

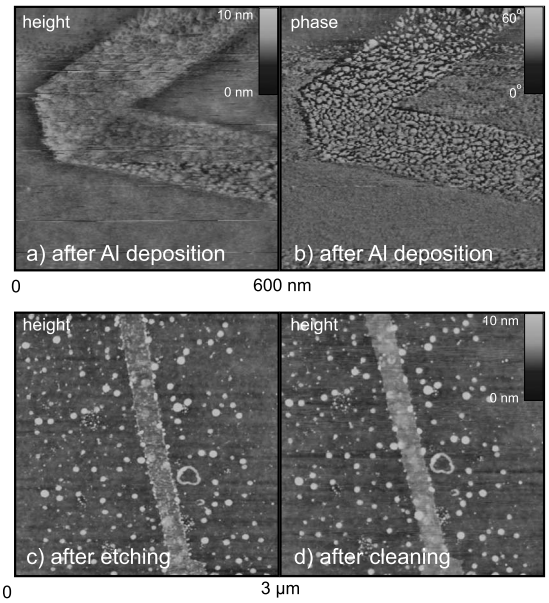

FIG. 2. AFM measurements of two graphene flakes. (a) and (b) Height and phase data (600×600 nm^2) for a type I device after the Al deposition step. (c) and (d) Height data (3×3 μm^2) for a type III device after etching and after annealing in Ar+H_2 atmosphere for about 2 h.

along the electrode length with a precision of about $1°-2°$. This could potentially result in shadowing effects due to the resist walls, yielding nonuniform deposition of Al in the patterned areas.

The type III devices were fabricated in order to investigate spin transport in narrow graphene ribbons. In this case all samples have the AlOx layer only underneath the Co contacts (same as type II). However, narrow flakes are difficult to spot under an optical microscope. To fabricate devices with widths down to 100 nm, somewhat larger flakes were selected and then oxygen plasma etched, prior to the definition of the composite AlOx/Co electrodes. The oxygen plasma etching step often resulted in a contaminated surface. Even though after etching the flakes were annealed in an Ar(95%):H_2(5%) atmosphere at 350° for about 2 h, large particles of unknown chemical composition still remain on the surface [see Figs. 2(c) and 2(d)].

The electrical measurements were performed using a standard ac lock-in technique ($f\leq17$ Hz) in the four-terminal nonlocal geometry. The ac current ($1-20$ μA) was set between a pair of electrodes and the in-phase ac nonlocal voltage was measured between the other pair of electrodes (see Sec. III A). All the room-temperature measurements presented in this study were made with the sample inserted in a vacuum container, with a base pressure of $\sim5\times10^{-6}$ mbar measured close to the pump, placed in between the poles of a room-temperature electromagnet. The measurements were done in vacuum in order to reduce the hysteresis of the graphene resistance as a function of the gate voltage. In the case of atmospheric measurement conditions (not presented in this paper) and on a time scale of about 24 h, we observed a reduction in the spin signal, which was accompanied by an increase in the contact resistances. The low-temperature (4.2 K) measurements were performed using an Oxford cryostat (with the sample placed in a vacuum tide dip-stick pumped before cooling to a base pressure of about 5×10^{-3} mbar) and a superconducting magnet.

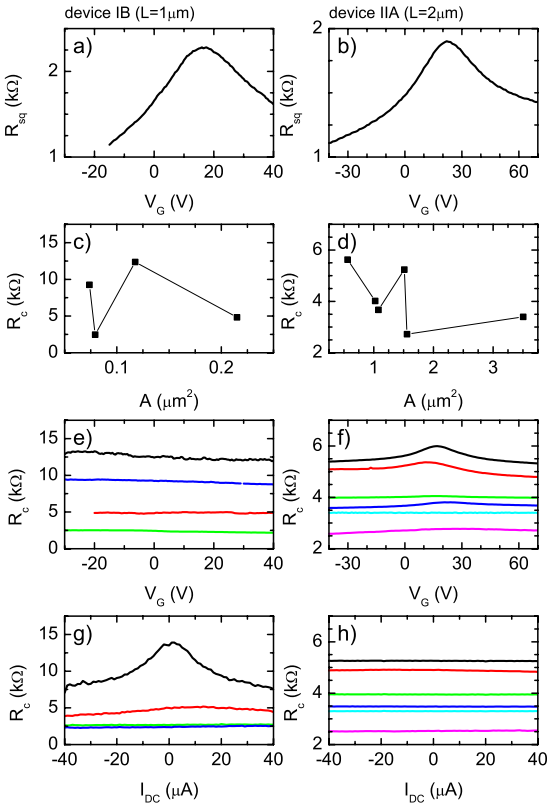

FIG. 3. (Color online) Room-temperature graphene and contact differential resistances dV/dI for a type I (left column) and a type II (right column) device, respectively. (a) and (b) Graphene square resistance R_{sq} as a function of the gate voltage V_G. (c) and (d) Contact resistance R_C vs contact area A. (e) and (f) R_C vs V_G. (g) and (h) R_C vs dc current bias I_{DC}.

In Fig. 3 we compare room-temperature electrical characteristics of graphene and contacts for two devices, one type I and one type II. As a function of the gate voltage, the four-terminal measurements of the graphene resistivity (top panels) show a maximum which corresponds to the Dirac neutrality point where the average charge density is equal to zero. At negative voltages with respect to the Dirac point position the conduction takes place via holes, whereas for positive voltages the conduction happens via electrons. The mobility of all samples presented in this study was in the range $2\times10^3-5\times10^3$ cm^2/V s. A clear correlation between the carrier mobilities of the type I (completely covered by aluminum oxide) and type II samples (oxide barriers only underneath the electrodes) could not be established. For the type III devices the carrier mobilities were about $2\times10^3-2.5\times10^3$ cm^2/V s.

In the lower panels of Fig. 3 we show three-terminal contact resistance measurements as a function of contact area [Figs. 3(c) and 3(d)], gate voltage [Figs. 3(e) and 3(f)], and dc current bias [Figs. 3(g) and 3(h)]. In general, the contact resistances of type I devices show a large spread in values and no clear scaling with the contact area. For the type II

samples, the spread is less and there seems to be some scaling of the contact resistance with the area. For the same nominal Al thickness and area the type I samples show larger contact resistances than the type II. For the type I devices the Co electrodes are defined on top the aluminum oxide layer which uniformly covers graphene. For the type II, aluminum and Co are deposited sequentially in the resist trenches at different evaporation angles. In this case, shadowing effects due to imperfect sample positioning may give rise to clean Co/graphene contact at the edge of the electrodes. Additionally, it is likely that the resist residues left on the aluminum oxide surface and on graphene are different. Randomly distributed resist residues cause a random effective contact area and therefore the scaling of the contact resistance with the area is lost. Type III samples revealed the largest spread of the contact resistance versus area (not shown). We attribute this to the dirty surface left after the etching process and to the ineffectiveness of the cleaning method (see the AFM images Fig. 2). For all types of contacts, a small and irregular gate voltage dependence of the contact resistance is recorded. Some low resistance contacts show a similar behavior to graphene, i.e., the contact resistance is higher when the graphene flake is at the charge neutrality point. Most likely, this indicates that part of the graphene layer contributes to the contact resistance. With respect to the dc bias current dependence, some high resistance contacts show high values in zero-bias conditions whereas low resistance contacts show very weak or no dc bias dependence. We note that the high differential resistance in zero dc bias conditions is not necessarily indicative of tunneling. Pinholes in the oxide may display the same behavior.[33] We take the large spread in the overall contact characteristics and the AFM measurements as evidence that the electrical characteristics of the contacts are determined by the current flowing through a random distribution of regions with increased transparency (thinner oxide layer or pinholes) or along grain boundaries, in contrast to the ideal case of tunnel barriers.

III. MODELING AND EXPERIMENTS

A. Graphene lateral spin valve devices

In Fig. 4(a) we show a schematic cross section of a lateral graphene type I spin valve device in the nonlocal measurement geometry.[34,35] For simplicity, we consider the outer electrodes (F1 and F4) as being nonmagnetic. The current set between F2 and F1 creates a spin accumulation (imbalance) in graphene at the position of F2, i.e., the electrochemical potentials for the spin-up and -down $(\mu_\uparrow, \mu_\downarrow)$ channels split[36] [Fig. 4(b)]. The spin accumulation $\mu_s = \mu_\uparrow - \mu_\downarrow$ diffuses away from the injection point $(x=0)$ and, in the linear regime, obeys the Bloch equation

$$D\nabla^2 \boldsymbol{\mu}_s - \frac{\boldsymbol{\mu}_s}{\tau} + \boldsymbol{\omega} \times \boldsymbol{\mu}_s = 0, \tag{1}$$

where D and τ represent the spin-diffusion constant and the spin-relaxation time, respectively. The term $\boldsymbol{\omega} \times \boldsymbol{\mu}_s$ describes the precession of the spin accumulation in an external magnetic field $\boldsymbol{B}$ with the Larmor frequency $\boldsymbol{\omega} = g\mu_B \boldsymbol{B}$, with

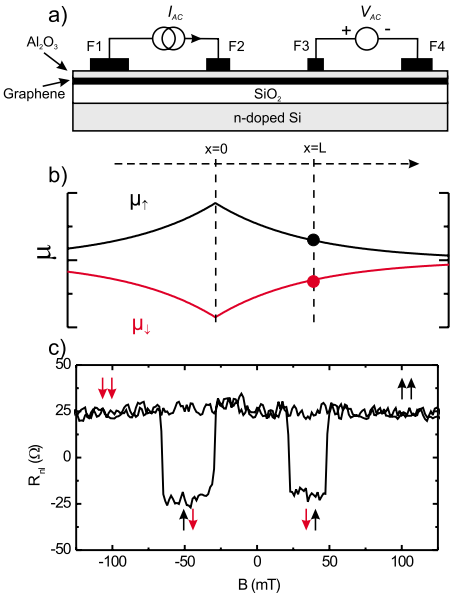

FIG. 4. (Color online) (a) Schematic cross section of a type I graphene spin valve device measured in the nonlocal geometry. (b) Representation of the electrical spin injection and detection process. (c) Spin valve measurement at room temperature and zero gate voltage for device IA with an injector-detector separation of 2.3 μm and a flake width of 500 nm. Note the 50 Ω spin signal, the sharp switching and the symmetry of the spin signal around zero nonlocal resistance.

$g=2$ as the gyromagnetic factor and μ_B as the Bohr magneton. In Eq. (1) we used a single relaxation time τ for reasons discussed later (see also Refs. 8 and 37).

The spin accumulation is probed nonlocally by the voltage difference V_{nl} between F3 and F4, with F3 placed at a distance $x=L$ on the order of λ with respect to the injection point. Depending on its magnetization orientation (parallel or antiparallel) with respect to the spin accumulation, electrode F3 is sensitive to the electrochemical potential of either the spin-up channel or the spin-down one [Fig. 4(b)]. The *spin signal* is defined as the nonlocal resistance $R_{nl} = V_{nl}/I$, where I represents the injection current. In the absence of precession $\boldsymbol{\omega} \times \boldsymbol{\mu}_s = 0$ the spin accumulation decays exponentially with the distance with the characteristic length $\lambda = \sqrt{D\tau}$, the spin-relaxation length. Under the assumption of high impedance contacts one can show that

$$R_{nl} = \pm \frac{P^2 R_{sq} \lambda}{2W} \exp\left(-\frac{L}{\lambda}\right), \tag{2}$$

where Eq. (1) from Ref. 35 has been adapted for the two-dimensional graphene. R_{sq} represents the graphene square (sheet) resistance, W is the width of the flake, and P is the spin injection and detection efficiencies of the ferromagnetic electrodes. The + (−) sign correspond to the parallel (antiparallel) orientation of the magnetization of the injector (F2) and the detector (F3). The spin valve measurement [see Fig. 4(c)] consists of monitoring the nonlocal resistance as a function of an external magnetic field which manipulates the relative orientation of the injector and detector magnetiza-

tions. The electrodes are engineered to have different widths so that, due to the shape anisotropy, they switch their magnetization orientation at different magnetic fields applied along their easy axis (the length). The *spin valve signal* $\Delta R_{nl}=2|R_{nl}|$ represents the change in resistance when the injector and detector magnetization configuration changes from parallel to antiparallel. The exponential dependence of the spin valve signal ΔR_{nl} on the injector-detector separation L allows for the extraction of the spin-relaxation length, the parameter of most interest.

In the nonlocal geometry, due to the separation of the injection and detection circuits, magnetoresistance effects related to the charged current flow, such as anisotropic magnetoresistance and Hall effects, do not superimpose on the spin signal. Theoretically, the nonlocal resistance is determined only by the spin accumulation injected at $x=0$ which diffused toward the detector ($x=L$), i.e., there are no other resistances (voltages) on top of the nonlocal resistance (voltage). In most samples, however, a small background (frequency and gate voltage dependent) is measured. In a local measurement geometry, the injection and detection circuits share the same pair of electrodes. The spin signals are superimposed on the graphene resistance (typically a few kΩ) and are more difficult to detect, especially if the contact or graphene resistance fluctuates. Nevertheless, there are a few local measurements reported.[3,5,12]

B. Modeling the contact resistance effects in the spin valve measurements

Analyzing Fig. 4(a) we see that the spins injected by F2 do not only diffuse symmetrically to the left and to the right in graphene, but can also return into the ferromagnetic electrode where they loose their initial orientation very fast (due to the strong spin-orbit coupling in the ferromagnet). Therefore, the magnitude of the spin accumulation created in graphene is drastically reduced if the contact resistance is much lower than the graphene resistance over one spin-relaxation length. This effect is known as the conductivity mismatch problem.[26] Taking into account the spin current drawn by the electrode (see the Appendix for details) one can show that

$$R_{nl} = \pm \frac{2P^2R_{sq}\lambda}{W}\frac{(R/\lambda)^2\exp(-L/\lambda)}{(1+2R/\lambda)^2-\exp(-2L/\lambda)}, \quad (3)$$

where the parameter R given by

$$R = \frac{R_C}{R_{sq}}W \quad (4)$$

represents spin relaxation due to the finite contact resistances R_C of the injector (F2) and detector (F3). In fact, R/λ represents the ratio between the contact resistance and the graphene resistance over one spin-relaxation length. Equation (3) is in agreement with Ref. 30 given our assumptions of negligible ferromagnet resistances with respect to the contact and graphene resistances and small polarizations P of the injector and detector electrodes.

In the limit of high impedance contacts ($R_C\to\infty$) Eq. (3) reduces to Eq. (2) as expected and the spin signal decays exponentially with the distance. Reducing the value of the relaxation parameter (i.e., of the contact resistance for given R_{sq} and W) the length dependence of the spin signal starts to deviate from the exponential form.[38] In the case of finite R_C and very long λ ($R/\lambda\to 0$) and short devices ($L\ll\lambda$), the nonlocal resistance is $\pm(P^2R_{sq}R^2)/(WL)$. Now, the spin signal is independent of λ; it depends on the injector detector spacing as $1/L$. Due to strong contact induced spin relaxation, spin transport is relevant only on the device length scale, the low impedance electrodes effectively cut the graphene flake with respect to the spin transport.

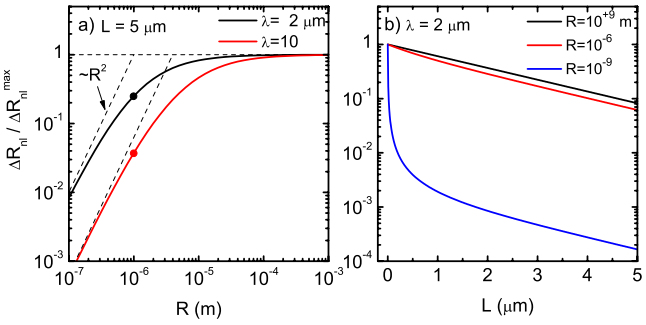

FIG. 5. (Color online) Calculations, according to Eq. (3), of the variation of the spin valve signal (normalized to the maximum spin signal ideally available) as a function of (a) the relaxation parameter R for two values of $\lambda=2$, 10 μm and (b) injector-detector separation L for $R=10^{+9}$, 10^{-6}, 10^{-9} m.

In Fig. 5(a) we plotted the variation of the nonlocal spin valve signal with respect to the relaxation parameter R for a device with an injector-detector separation $L=5$ μm and two values for λ: 2 and 10 μm, respectively. The signal is normalized to the value corresponding to infinite contact resistance. For given graphene properties, a variable R parameter represents a variable contact resistance R_C. The full circles in Fig. 5(a) correspond to $R=10^{-6}$ m (i.e., $R_C=1$ kΩ for typical values $R_{sq}=1$ kΩ and $W=1$ μm). Due to the conductivity mismatch, for $\lambda=2$ μm one measures only 25% of the totally available signal in the ideal case of high impedance contacts. For $\lambda=10$ μm, only 3.7% of the ideal signal is measured. The strong contact induced spin-relaxation regime is identified as the region where the signal is proportional to R^2. In Fig. 5(b) we show the variation of the spin signal with respect to the injector-detector separation for $\lambda=2$ μm and three values of the relaxation parameter. For $R=10^{-9}$ m and $L\leq\lambda$ the spin signal depends on the injector-detector separation as $1/L$.

We note that tunnel barriers appear as a natural solution to the conductivity mismatch problem for the following two reasons. First, the tunneling current is proportional to the density of states on the either side of the barrier. This implies that the spin polarization of the current present in the ferromagnetic Co is maintained when injected in graphene. Second, the tunnel barrier, if not too transparent, may block the back flow of spins into the Co electrode. Whether the spin injection takes place via tunneling or pinholes it does not modify our model. The contact induced spin relaxation is given by the ratio between the contact resistance and the graphene resistance over one spin-relaxation length.

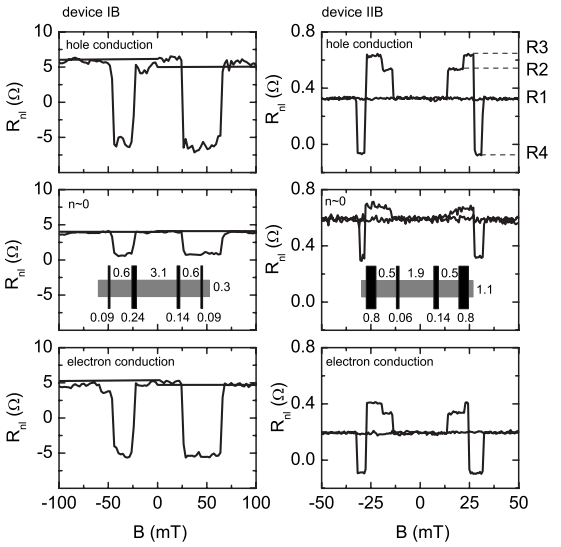

FIG. 6. Spin valve measurements at room temperature for a type I device (left column) and a type II device (right column). Device dimensions are given in the insets in micrometers. For the Dirac point (middle panels) the spin signals are smaller than for metallic regimes (densities of $2\times10^{12}-3\times10^{12}$ cm^{-2}). The y scales have the same span for each device. The resistance levels R1, R2, R3, and R4 observed for the device IIB are due to the magnetic configuration of all four electrodes (see Fig. 7 and the text).

C. Graphene spin valve measurements

In this section we discuss general characteristics of the spin valve measurements. In Fig. 6 we show measurements for a type I and a type II device for three charge-density regimes: zero charge density (Dirac neutrality point) and metallic hole and electron densities of $2\times10^{12}-3\times10^{12}$ cm^{-2}. Due to the different contact separations, carrier mobilities, and metallic charge densities, a direct comparison between these measurements is not trivial. In general, we observe large signals (few Ω up to 50 Ω) for the type I devices, whereas for the type II the spin signals were a few tenths of an ohm up to a few ohms. We identify two reasons for this difference. First, for the type I devices the contact resistances were in the order of 10–200 kΩ, whereas for the type II the contact resistances were always lower, on the order of 1–10 kΩ. As already discussed the low impedance contacts induce significant spin relaxation, which severely reduces the magnitude of the spin signal. Second, the measurements are consistent with relatively high spin injection and detection efficiencies (P=10–20 %) in the case of high impedance contacts, whereas for low impedance contacts the efficiencies were on the order of 3–5 %.

For the type II device in Fig. 6 we observe four resistance steps which we associate with the magnetization switching of all four electrodes, graphically shown in Fig. 7. Let us consider that for high positive magnetic field the magnetization of all electrodes points in the "up" direction and that F2 injects spin up carriers in graphene. At F1, where the current flows from graphene to F1, spin-down injection takes place. This partially cancels the spin-up accumulation created by F2. Both F3 and F4 electrodes probe the spin-up channel and

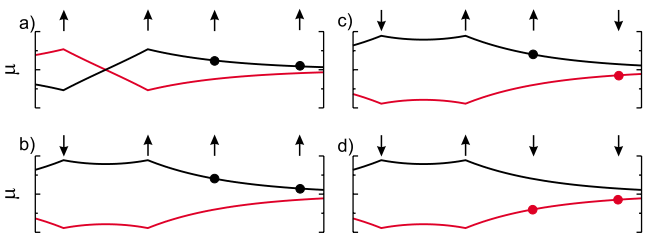

FIG. 7. (Color online) Schematic representation of the electrochemical potentials for the spin-up and -down channels as a function of distance for device IIB in Fig. 6. The magnetic configurations of all four ferromagnetic electrodes (which give the multiple resistance levels R1, R2, R3, and R4) and the electrode positions are indicated by the arrows.

a positive nonlocal voltage (resistance) is measured since F3 is closer to the injectors than F4 [Fig. 7(a)]. Ramping down the field toward −50 mT the electrodes switch their magnetization in the reverse order of their width: F1, F4, F3, and F2. When F1 changes its magnetization orientation, both F1 and F2 inject spin-up carriers and the total spin accumulation increases causing a positive change in R_{nl} [Fig. 7(b)]. Next, the detector F4 switches, probing the spin-down channel, and the nonlocal voltage difference increases again [Fig. 7(c)]. At around −25 mT, F3 switches its magnetization. Now, both injectors inject spin-up carriers whereas the detectors probe the spin-down ones, which causes R_{nl} to become negative [Fig. 7(d)]. The last switch is that of F2. This configuration (not shown) is equivalent to the starting one with all magnetizations pointing down now and the starting level of nonlocal resistance is recovered.

The four changes in the nonlocal resistance point out that the spin-relaxation length in graphene is at least on the order of the F1-F3 or F4-F2 distances (~2.9 μm for this sample) since otherwise the resistance step due to F1 or F4 switching their magnetization would not be observed. Additionally, the spin accumulation can extend underneath all contacts, which means that the aluminum oxide barriers are not too opaque or too transparent. In the next sections we extract quantitative information regarding the spin-relaxation length λ.

D. Length dependence of the spin signal

Equation (3) can be used to extract λ from the length dependence of the spin signal. Ideally, all one has to do is to make a series of devices which should strictly meet the following conditions. First, the F1 and F4 electrodes do not contribute to the measurement; they are either placed at distances much larger than λ with respect to F2 and F3 or they are replaced with nonmagnetic ones. Second, F2 and F3 should have identical spin injection and detection efficiencies and resistances from device to device. In addition, all the graphene flakes should have identical transport properties (same carrier mobility) and the same width (in case that enhanced spin relaxation takes place at the device edges). The samples should be processed and measured in identical conditions since it is not actually known how the substrate could influence the spin relaxation. If all these conditions are met, then the only variable left is the spacing between the injector

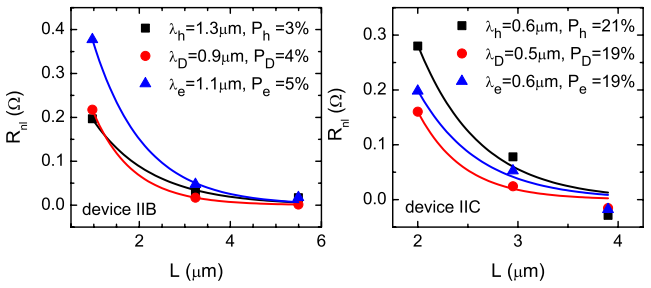

FIG. 8. (Color online) Length dependence of the spin signal as extracted from the magnitude of the multiple resistance levels observed in spin valve measurements (type II devices at room temperature) for three conduction regimes: $n \sim 0$ and hole and electron densities of $2\times10^{12}-3\times10^{12}$ cm^{-2}. For these samples we calculated an average R parameter of $1\times10^{-6}-2\times10^{-6}$ m. The spin-relaxation lengths are higher in the metallic regime [subscript e (h) is for electron (hole) conduction] than at the Dirac neutrality point (subscript D). The injector and detector efficiencies are also indicated. For the spin valve measurements of device IIB, see Fig. 6.

and the detector electrodes. This has to be varied systematically, so that the application of Eq. (3) would allow one to extract λ and P. Experimentally some of these conditions can be fairly met (especially if several devices can be fitted on the same flake), except controlling the polarization of the electrodes and the reproducibility of contact resistance which are probably the most important parameters. In spite of these problems we have been able to show some consistent behaviors for samples where the contact resistances were more uniform[8] [see also Fig. 10(a)].

In this paragraph we show how the multiple resistance steps, which are due to ferromagnetic electrodes placed at various distances, can be used for a quantitative estimation of λ. For the all up magnetization configuration which gives the resistance level R_1 [Figs. 6 and 7(a)] the spin accumulation present at the position of the voltage probe F3 is just the sum of two spin accumulations of opposite sign produced by F2 and F1, which have decayed exponentially with the distance (F2-F3 and F1-F3). We neglect here the spin relaxation induced by electrode F2 on the spin accumulation produced by F1 and detected by F3. Similar arguments apply for the detector F4 but the exponential decays are for larger distances. Additionally, we note that some measurements (including this one) show a gate-voltage-dependent background resistance (which we denote as R_0). Note that, theoretically, the spin signals R_2 and R_4 should have identical values but opposite signs [see Figs. 7(b) and 7(d)]. Therefore, we can write $R_1=[+R_{23}-R_{13}]-[+R_{24}-R_{14}]+R_0$, where R_{23} is the resistance level produced by the F2-F3 injector-detector pair which are placed at the distance L_{32} and so on. Applying a similar reasoning for R_2, R_3, and R_4 we obtain a system of four equations with five unknowns R_{23}, R_{13}, R_{24}, R_{14}, and R_0. In this sample the F1-F3 and F2-F4 distances were virtually equal ($\sim$2.9 μm) so by taking $R_{13}=R_{24}$ we can solve the system of equations and extract the length dependence of the spin signal from a single measurement. The same analysis has been performed for another sample. The results are plotted in Fig. 8 together with fits according to Eq. (3). The fits reveal a spin-relaxation length on the order of 1 μm, which is somewhat higher in the metallic regime than for the zero-charge-density regime.

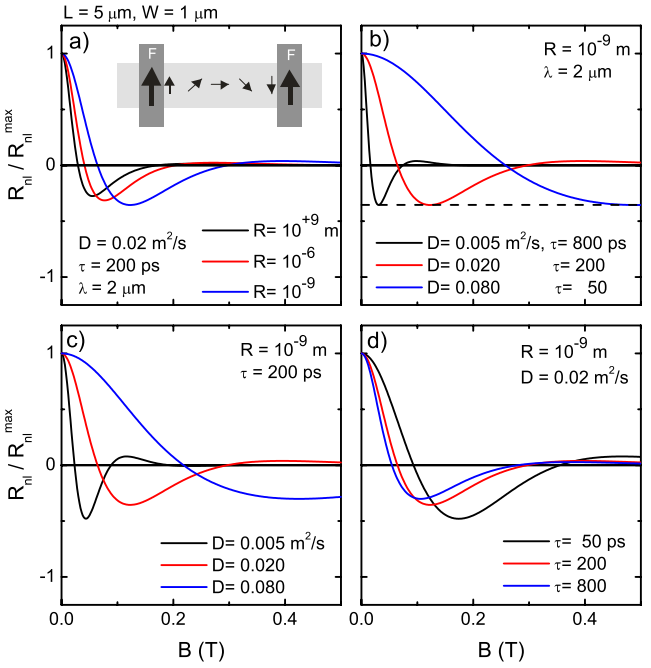

FIG. 9. (Color online) Calculations of the spin precession curves for various values of R, D, and λ. Only the parallel magnetization of the injector and detector electrodes case is shown for positive values of the perpendicular magnetic field. See text for details.

E. Modeling the contact resistance effects in the spin precession measurements

In this section we discuss the effect of the contact impedance on the spin precession measurements. Let us consider a spin valve device in which the ferromagnetic injector and detector electrodes have their respective magnetizations oriented parallel and a magnetic field B_z, smaller than what is required to pull the magnetization of ferromagnetic electrodes out of plane, is applied perpendicular to the sample plane. In this situation, the injected spins undergo precession (Hanle effect) while diffusing from the injector toward the detector [see the schematics of the inset in Fig. 9(a)]. The detector signal oscillates with B_z. The signal is maximum at $B_z=0$ (no precession), vanishes at fields which correspond to an average spin precession angle of 90° and it is minimum when the spins have precessed an average angle of 180°. In Fig. 9 we present several calculated precession signals for various values of the relaxation parameter R, the diffusion constant D, and the spin-relaxation time τ. All relevant parameters are indicated in the figures. To allow comparison the signals have been normalized to the maximum value. We refer to the Appendix for modeling details. Next, we analyze the shape of the curves with respect to their width, defined by the 90° precession angle, and the amount of overshoot, defined as the ratio between the minimum and the maximum values of the signal (180° and 0° precession). In Fig. 9(a) we plotted the precession signal for three values of R and for fixed D and τ (values close to the ones corresponding to our

samples). With decreasing the relaxation parameter R, i.e., decreasing the contact resistance for given graphene properties, the precession curve becomes broader and the overshoot increases in magnitude. Of interest is to determine how R, D, τ influence the shape of the precession curve and whether one can accurately extract the spin-relaxation time in the case of very low impedance contacts, for example, $R_C = 1\ \Omega$, which for $R_{sq} = 1\ \text{k}\Omega$ and $W = 1\ \mu\text{m}$ corresponds to $R = 10^{-9}$ m.

In Fig. 9(b) we show three curves for which $R = 10^{-9}$ m and the values for D and τ are such that they give a constant spin-relaxation length of 2 μm. This plot indicates that the overshoot depends only on λ. Extensive analysis reveals that for a given injector-detector distance L and for $\lambda \lesssim L$, the overshoot depends only on λ and R; it does not depend on the individual values of D and τ as long as they produce the same λ. Therefore, for a given sample (for which L and R are known) the spin-relaxation length can be estimated just by quantifying the amount of the overshoot. In Figs. 9(c) and 9(d) we plotted spin precession signals by varying either D or τ while keeping the other parameters constant. For a given τ, the precession curve is wider for a higher D. This can be simply understood by the fact that, for a higher D (i.e., a higher carrier mobility), a stronger magnetic field is required to induce 90° precession since it takes less time for the spins to diffuse the fixed injector-detector distance. Figure 9(d) shows wider precession curves for smaller spin-relaxation times. For high relaxation times, the shape of the curves is essentially the same. This can be understood by the fact that most of the injected spins do not relax before reaching the detector and the angle of precession is mainly determined by the time it takes them to arrive at the detector, i.e., the diffusion constant and the device length. For low spin-relaxation times, the spins following a long diffusive path have a high chance to relax before reaching the detector and, therefore, do not contribute to the measured signal. In this case, the spin signal is mainly determined by the spins following a short diffusive path, and which arrive faster at the detector (effectively having a higher diffusion constant). The overall behavior is that, for given device characteristics and dimensions, the precession measurements allow accurate extraction of the spin transport properties provided that the contacts do not induce strong spin relaxation, i.e., the relaxation parameter R is comparable or higher than the spin-relaxation length.

F. Spin precession experiments

In Fig. 10(a) we show the length dependence of the spin valve signal for three type I devices made on the same graphene flake measured at 4.2 K in the metallic hole conduction regime $n(h) \sim 2 \times 10^{12}$ cm^{-2}. For this sample the contact resistances were more uniform (1–2 kΩ). The measurements indicate a spin-relaxation length of 1.6 μm. In Fig. 10(b) we present a spin precession measurement for a 5-μm-long device from the same batch of samples. The fit of the low B field part of the precession curve indicates a spin-relaxation length of 1.4 μm, in very close agreement with the length dependence measurement. This indicates that the

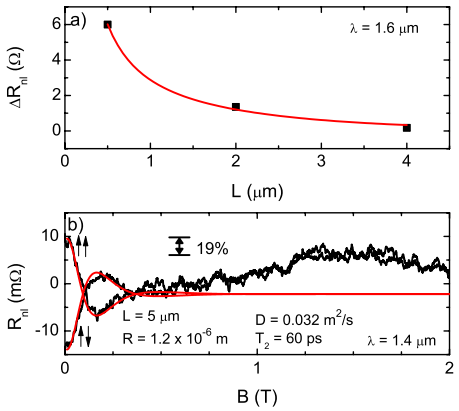

FIG. 10. (Color online) Measurements at 4.2 K in the metallic hole regime, $n(h) \sim 2 \times 10^{12}$ cm^{-2}, type I devices. (a) Length dependence of the spin valve signal and fit according to Eq. (3) corresponding to a spin-relaxation length of 1.6 μm. (b) Experimental spin precession curves for both parallel ($\uparrow\uparrow$) and antiparallel ($\uparrow\downarrow$) magnetization orientations of injector and detector electrodes. The (red) lines represent fits with the parameters D and τ indicated in the figure. The change in the spin signal is consistent with a 19% reduction in the spin-relaxation time for spins injected perpendicular to the graphene plane compared with spins injected in the graphene plane.

longitudinal and transversal relaxation times (T1 and T2) are similar for these devices.[8] Therefore, we argue that the precession measurements can be used to determine the spin transport properties (τ, λ) of graphene. The advantage over the difficult to realize length dependence of the spin signal (due to the irreproducibility of the contact resistances or the spin injection and detection efficiencies) is obvious: the fabrication and proper characterization of a single device.

With increasing the perpendicular magnetic field above 0.5 T the magnetization of the Co electrodes is slowly pulled out of plane. For fields above 1.25 T the relative orientation of the magnetization of the Co electrodes is parallel (both magnetizations are completely out of plane). Now, the injected and detected spins are perpendicular to the two-dimensional plane of the graphene layer and parallel to the external field (no precession takes place). We observe that the spin signal is somewhat lower than the zero field signal, when the orientation of the injected and detected spins is parallel with the sample plane. The difference in the magnitude of the signal corresponds to a relaxation time $\tau_\perp$ smaller by $\simeq 20\%$ than $\tau_\parallel$. Similar room-temperature experiments not shown here support these low-temperature spin anisotropy measurements. This indicates that the effective magnetic fields responsible for the spin relaxation lie mostly in the two-dimensional plane of graphene. For a full discussion we refer to Ref. 8. However, we note that in the case of Rashba- or Dresselhaus-type spin-orbit interaction the effective spin-orbit fields lie exclusively in the graphene plane, and theoretical calculations indicate that $\tau_\perp = (1/2)\tau_\parallel$.[37]

In Fig. 11 we show room-temperature spin precession measurements for a type I sample (contact resistances $R_C = 20$–40 kΩ, a charge-carrier mobility $\mu = 2.4 \times 10^3$ cm^2/V s, and a width $W = 0.3$ μm) and a type II sample ($R_C = 1$–2 kΩ, $\mu = 5 \times 10^3$ cm^2/V s, and

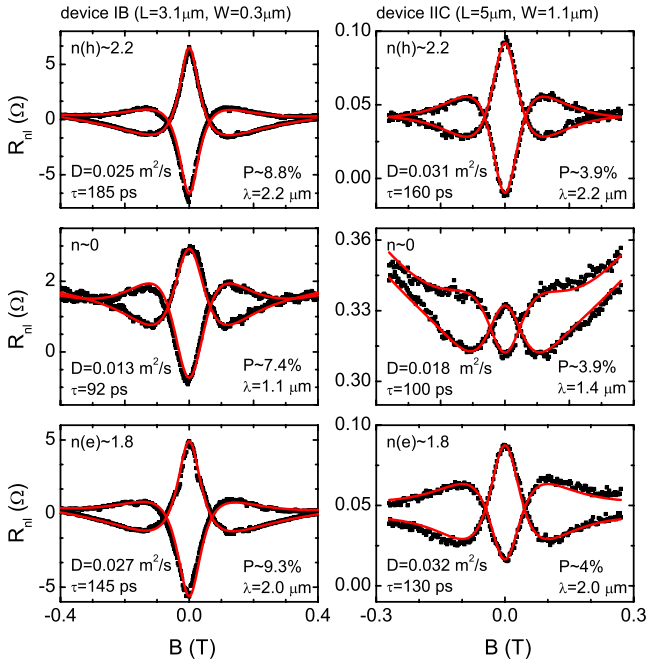

FIG. 11. (Color online) Room-temperature spin precession measurements and fits (red lines) for parallel and antiparallel magnetization orientations of the injector and detector electrodes. Three different conduction regimes are shown on the left column for a type I device (with R_C=20–40 kΩ, μ=2.4×10^3 cm^2/V s) and on the right column for a type II device (R_C=1–2 kΩ, μ=5×10^3 cm^2/V s). The carrier concentrations, in units of 10^{12} cm^{-2}, the flake dimensions, and the fit parameters (D, τ, and P) are indicated in the figures.

W=1.1 μm) for similar charge-carrier type and density. The fits indicate a higher spin-diffusion constant for device IIC than for device IB (reflecting the higher carrier mobility) and similar spin-relaxation times. The injection and detection efficiencies of device IB are somewhat higher than for device IIC. The spin-relaxation lengths, calculated according to $\lambda = \sqrt{D\tau}$, are also displayed. Given the different charge-carrier mobilities and widths of the two devices, a direct comparison of the spin-relaxation times may seem inappropriate. We note, however, that previous experiments on type I devices with charge-carrier mobilities on the order of μ=2×10^3–3×10^3 cm^2/V s indicate spin-relaxation times of 60–170 ps.[3,8] In this respect the spin-relaxation times of device IIB fall in the same range as the ones measured for the type I devices. Therefore, we can only conclude that for a range of carrier mobilities of μ=2×10^3–5×10^3 cm^2/V s and for device widths on the order of 0.3–1 μm the presence of the aluminum oxide layer on top of graphene does not influence the spin transport properties. The situation may change if the carrier mobilities or the device widths could be varied significantly. The gate voltage dependence is summarized in Sec. III H.

G. Spin precession in graphene ribbons

In this section we discuss room-temperature spin precession measurements for structures down to 100 nm in width

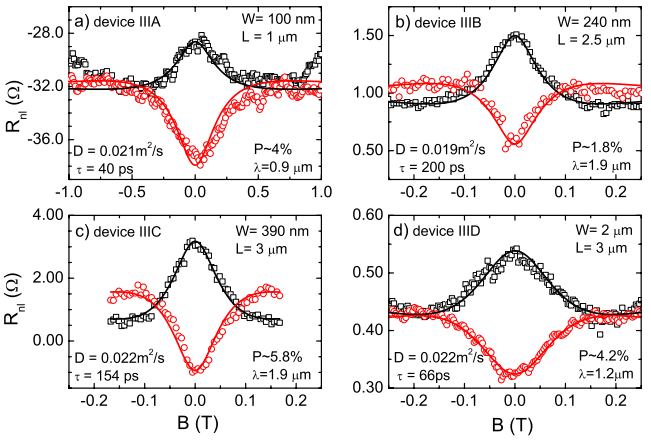

FIG. 12. (Color online) Room-temperature spin precession measurements and fits, parallel (black) and antiparallel (red) relative orientation of the injector and detector magnetizations, in the metallic hole conduction regime $n(h) \sim 2\times10^{12}$ cm^{-2} for four type III devices of different widths. The device dimensions (width W and length L) and the fit parameters are indicated in the figure.

(type III devices). These measurements were performed in order to establish whether the relatively short spin-relaxation times (compared with the theoretical predictions) may be due to enhanced spin-flip processes taking place at the edges of the graphene flake. The fabrication procedure involved an oxygen plasma etching step and it was described in Sec. II. In order to exclude possible effects related to the fabrication procedure and realize a proper comparison of the spin transport properties in a set of devices which differ only in width, all these devices were fabricated by etching. The values of the contact resistances for this type of etched structures show poor reproducibility compared with the type I and II devices (not shown). We attribute this to the unknown residues produced during the etching process which hinders making proper contacts to graphene. Additionally, the charge-carrier mobilities in these samples were on the order of 2×10^3–2.5×10^3 cm^2/V s, being the lowest we have measured so far. This may be attributed to the residues created during the etching step.

In Fig. 12 we show a set of four precession measurements in the metallic hole conduction regime performed on devices with widths of 0.10, 0.24, 0.39, and 2 μm. In the order of increasing the graphene flake width the spin-relaxation times read 40, 200, 154, and 60 ps, respectively. In spite of similar charge transport properties, i.e., similar spin-diffusion constants, the spread in the spin-relaxation times is rather large. No clear scaling behavior with the device width is found. Although the 40 ps spin-relaxation time for the 100-nm-wide device is the lowest we measured in any of our devices, a definitive conclusion with respect to a presumably strong spin relaxation at the device edges cannot be drawn. Spin-relaxation times of 50–60 ps were measured for relatively wide flakes as well. The diffusion constant in two dimensions is given by $D=v_F l/2$, with v_F as the Fermi velocity and l as the mean free path. For D=0.02 m^2/s and $v_F \sim 10^6$ m/s we find $l \sim 40$ nm, which in all cases is shorter than the device width W. Therefore, for $W \gg l$ it may be expected that the device edges play a minor role with

respect to the spin relaxation. For some precession curves there are a few sets of parameters that describe reasonably the experiment. In that case we fixed the spin-diffusion constant to the charge-diffusion constant,[39] leaving the spin-relaxation time as the only relevant fitting parameter. Generally, the spin valve signals at the Dirac point were too small to produce a useful precession curve. The gate dependence of the spin signals for devices IIIA and IIIB is discussed in the next section.

H. Gate-voltage-dependent spin transport

In Figs. 6 and 11 we presented spin valve and spin precession measurements for a type I and a type II device for three charge densities (gate voltages). Gate voltage scans of the spin signal for type I devices have been presented in Refs. 3 and 8. More recently, the gate voltage dependence of the charge- and spin-diffusion constants has been discussed in Ref. 39. In this section we summarize the gate voltage dependence of the spin transport measurements with the focus on the graphene ribbons.

In Fig. 13 we show measurements for device IIIA (100 nm wide) on the left column and for device IIIB (240 nm wide) on the right column. In Figs. 13(a) and 13(b) we present spin valve measurements (in the hole conduction regime). The gate voltage dependence of the graphene square resistance is shown in Figs. 13(c) and 13(d). The variation of the spin valve signal ΔR_{nl} with the gate voltage, as extracted from the gate voltage scans of the parallel and antiparallel nonlocal resistances, is presented in Figs. 13(e) and 13(f). Although relatively noisy, we note that the spin valve signal is smaller for zero-charge-carrier density than for the metallic regimes. This is a general characteristic for all types of devices we investigated. Recalling Eq. (3) we see that for a given device (i.e., given width W and length L) the magnitude of the spin signal depends on the injector and detector efficiencies P, the spin-relaxation length λ, the graphene square resistance R_{sq}, and the contact resistance R_C (through the relaxation parameter $R=R_C W/R_{sq}$), which all can be gate voltage (charge density) dependent. In the following we attempt to extract information on the variation of λ with respect to the gate voltage. The measurements presented in Figs. 8 and 11 reveal a weak dependence of P with the gate voltage. Even though not measured for these devices we assume no V_G dependence of the contact resistances based on measurements presented in Fig. 3. The injector and detector contact resistances measured for $V_G=0$ V were 49 and 72 kΩ for device IIIA and 9 and 20 kΩ for device IIIB. The variation of the relaxation parameter with V_G is therefore given by the variation of R_{sq} with V_G shown in Figs. 13(c) and 13(d). By applying Eq. (3) one can calculate the variation of the spin-relaxation length as a function of V_G from the variation of the spin signal with V_G. The result of this calculation is presented in Figs. 13(g) and 13(h). Clearly, the spin-relaxation length is smaller for gate voltages corresponding to the charge neutrality point. In the next paragraph we look at the spin-relaxation mechanism and provide the explanation for this dependence.

The spin-relaxation length depends on the spin-relaxation time and the (spin) diffusion constant through $\lambda=\sqrt{D\tau}$. A

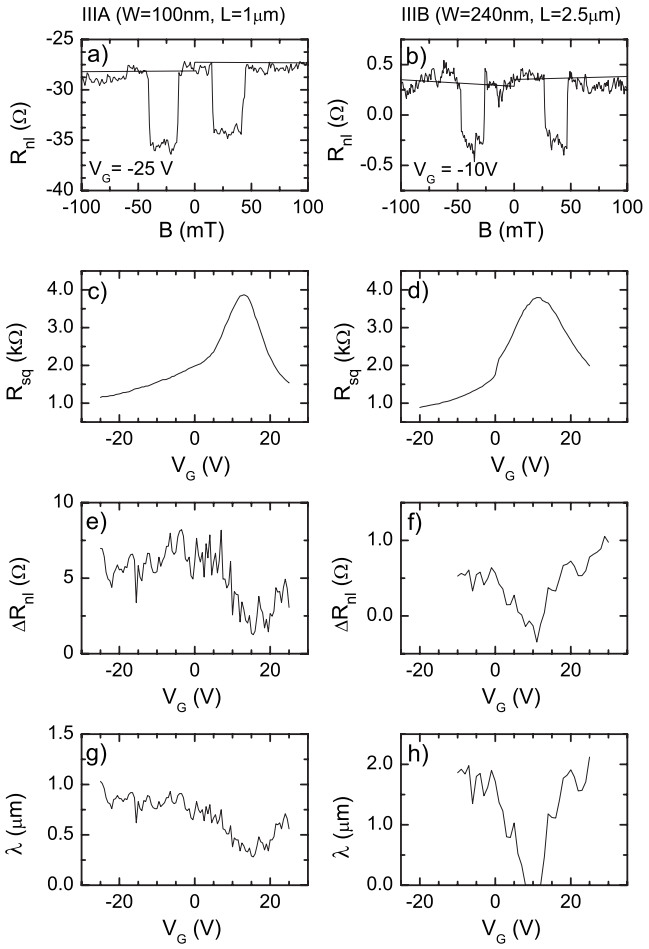

FIG. 13. Spin and charge measurements at room temperature for device IIIA (100 nm wide) and for device IIIB (240 nm wide): (a) and (b) spin valve measurements in the hole conduction regime, (c) and (d) graphene square resistance as a function of the gate voltage (V_G), and (e) and (f) the spin valve signal ΔR_{nl} vs V_G. (g) and (h) represent the calculation of the spin-relaxation length from the magnitude of the spin signal [using Eq. (3)] as a function of V_G (see text for details).

variation of D and/or τ with the gate voltage attracts a gate voltage dependence of λ. The diffusion constant in graphene depends on the charge-carrier density being smaller for the Dirac point than in the metallic regime. Additionally, depending on the spin-relaxation mechanism, the spin-relaxation time varies with the momentum-relaxation time τ_e (or charge-carrier mobility). Since $D=v_F^2\tau_e/2$, τ depends on D. In the case of the Elliott-Yafet mechanism the spins are randomized with a certain probability at each scattering event.[40,41] This determines that $\tau \propto \tau_e$ ($\tau \propto D$). In contrast, for the D'yakonov-Perel' mechanism[42,43] the spin orientation is lost by random spin precession taking place between scattering events. In this case $\tau \propto \tau_e^{-1}$ (i.e., $\tau \propto D^{-1}$). In Fig. 14(a) we summarize the dependence of the spin-relaxation time on the diffusion constant from the precession measurements presented in Refs. 3 and 8 and this work (Figs. 11 and 12). The spin-relaxation times increase slightly with the diffusion constant. Given the large variation registered from device to device and the small range over which the diffusion constant

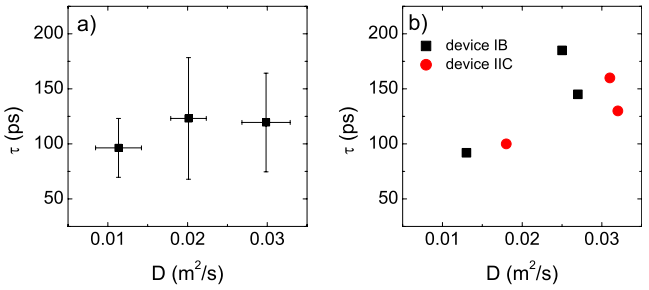

FIG. 14. (Color online) The spin-relaxation time as a function of the spin-diffusion constant at room temperature: (a) summary of all the spin precession measurements presented in this study and Refs. 3 and 8 and (b) the dependence for devices IB and IIC as extracted from Fig. 11.

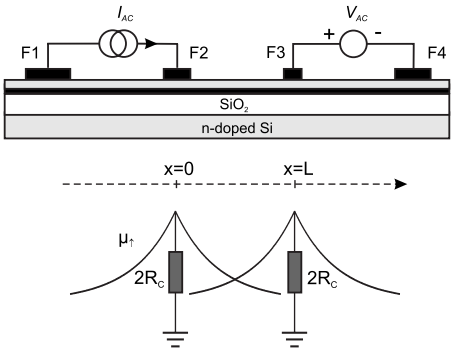

FIG. 15. Modeling of the spin relaxation via the contacts. F1 and F4 are considered as nonmagnetic.

(i.e., the mobility) varies, a definitive conclusion cannot be drawn from this plot. In Fig. 14(b) we show the dependence of τ on D extracted from Fig. 11. A clear trend of increasing τ with D is observed suggesting that the spin scattering mechanism for our samples is of Elliott-Yafet type. Therefore, in cleaner graphene systems larger spin-relaxation times are expected. Worth mentioning is that for a carrier mobility a factor of 100 higher, such as in suspended devices, the spin-relaxation length would increase by a factor of 10 even if the spin-relaxation times would remain in the 100–200 ps range. Given the trend we observe in Fig. 14 that the prospect of realizing spin transport in graphene over tens of microns seems to be within reach.

IV. CONCLUSIONS

We have successfully realized all electrical injection and detection of spin accumulation in graphene at room temperature and 4.2 K. The conductivity mismatch problem has been partially overcome by the introduction of a thin aluminum oxide layer between the metallic Co electrodes and the semiconducting graphene. By proper modeling, we have taken into account the spin relaxation induced by the contacts. From the length dependence of the spin valve signal and spin precession measurements, we have shown that the longitudinal (T_1) and the transversal (T_2) spin-relaxation times are similar. The anisotropy in the spin-relaxation times $\tau_\parallel$ (spins injected parallel to the graphene plane) and $\tau_\perp$ (spins injected perpendicular) reveal that the effective magnetic fields due to the spin-orbit interaction lie mostly in the two-dimensional graphene plane. For the 2×10^3–5×10^3 $\mathrm{cm}^2/\mathrm{V\,s}$ carrier mobilities of our samples, we found spin-relaxation times of 50–200 ps. These relatively short relaxation times are not determined by enhanced spin-flip processes taken place at the devices edges, for structures of 2 μm down to 100 nm in width. The presence of the aluminum oxide covering the graphene flakes in some experiments does not influence the relaxation times significantly. Room-temperature and 4.2 K measurements indicate similar spin transport properties. The linear dependence of the spin-relaxation time on the momentum scattering time indicates that the spin-relaxation mechanism is Elliott-Yafet type. The gate voltage dependence of the spin signal and precession experiments show better spin transport properties in the metallic regime than at the charge neutrality point. Extrapolating our results to carrier mobilities a factor of 100 higher, spin-relaxation lengths on the order of tens of micrometers are expected.

Finally, we note that the range of carrier mobilities of our samples was rather limited. Most likely, the mechanisms limiting the charge-carrier mobilities also limit the spin-relaxation times. In this respect, it would be interesting to study spin transport properties for devices with significantly larger carrier mobilities, such as suspended devices, where the mean free path would also become comparable or higher than the device dimensions.

ACKNOWLEDGMENTS

We would like to acknowledge B. Wolfs, S. Bakker, J. Baas, and J. Buurma for technical support. This work was financed by MSC^{plus}, NanoNed, NWO (via a "PIONIER" grant and a "Top Talent" grant) and FOM.

APPENDIX: MODELING OF SPIN RELAXATION INDUCED BY THE CONTACTS

We consider the geometry shown in Fig. 15 with F1 and F4 being nonmagnetic. The injector F2 and the detector F3 are placed at the distance L. In the frame of the two-channel current model the current is carried by two independent channels, a spin-up and a spin-down one. In the absence of external magnetic fields the spin accumulation is constant in the y and z directions; only the x component varies with the distance. To simplify the mathematical description we consider symmetric splitting of the electrochemical potentials of the two spin species and discuss only the spin-up channel. Neglecting the linear term due to charge current flow for $x<0$, the solutions for the spin-up electrochemical potential in the x direction are of the form

$$\mu_\uparrow(x) = a\,\exp\left(+\frac{x}{\lambda}\right), \quad \text{for } x<0,$$

$$\mu_\uparrow(x) = b\,\exp\left(-\frac{x}{\lambda}\right) + c\,\exp\left(+\frac{x}{\lambda}\right), \quad \text{for } 0<x<L,$$

$$\mu_{\uparrow}(x) = d\exp\left(-\frac{x}{\lambda}\right), \quad \text{for } x > L.$$

Considering parallel orientation of the magnetization of the injector and detector electrodes and the same polarization P for the injector and detector electrodes, we write the nonlocal resistance as

$$R_{nl}(L) = \frac{P}{I_{ac}}\frac{\mu_{\uparrow}(L)}{e} = \frac{P}{I_{ac}}\frac{d\exp(-L/\lambda)}{e}, \tag{A1}$$

where we took into account the symmetric splitting $\mu_{\uparrow}(L) = -\mu_{\downarrow}(L)$ when applying Eq. (2) from Ref. 44. The constants a,b,c,d are determined from the boundary conditions. The continuity of the spin-up electrochemical potential at $x=0,L$ gives the following two equations:

$$a = b + c, \tag{A2a}$$

$$b\exp\left(-\frac{L}{\lambda}\right) + c\exp\left(+\frac{L}{\lambda}\right) = d\exp\left(-\frac{L}{\lambda}\right). \tag{A2b}$$

The spin relaxation via the contacts is taken into account when writing the spin current conservation equations as explained in the following. The ferromagnet F2 injects a spin-polarized current in graphene via tunnel barriers of resistance R_C with an efficiency P. The total injected spin current is $I_s(0) = PI_{ac}$ and the total spin-up current available is half, $I_{\uparrow}(0) = PI_{ac}/2 = I_x(0)$. The spin-up current $I_x(0)$ diffuses to the left and to the right in graphene or flows back into the contact. The spin-up current flowing in graphene is written in the form $I_G^{\uparrow} = \pm(\sigma/2)W(1/e)d\mu_{\uparrow}/dx$. Here, e is the electron charge, and σ and W are the conductivity and the width of the graphene flake. The (unwanted) spin-up current through the contact is written as $I_C^{\uparrow} = (1/R_C^{\uparrow})\mu_{\uparrow}/e \approx (2eR_C)^{-1}\mu_{\uparrow}$. Here, we have considered $R_C^{\uparrow}(=R_C^{\downarrow}) \approx 2R_C$, with $R_C^{\uparrow}$ as the effective resistance the up spins encounter when going back into contact. The spin current conservation equations at $x=0,L$ read

$$P\frac{I_{ac}}{2} = a\frac{\sigma W}{2e\lambda} + b\frac{\sigma W}{2e\lambda} + c\frac{\sigma W}{2e\lambda} + \frac{a}{2eR_C}, \tag{A3a}$$

$$0 = b\frac{\sigma W}{2e\lambda}\exp\left(-\frac{L}{\lambda}\right) + c\frac{\sigma W}{2e\lambda}\exp\left(+\frac{L}{\lambda}\right) - d\frac{\sigma W}{2e\lambda}\exp\left(-\frac{L}{\lambda}\right) + \frac{d}{2eR_C}\exp\left(-\frac{L}{\lambda}\right). \tag{A3b}$$

Here, we have used the fact that the spin current flowing away from the contact (the exponential decaying electrochemical potential from the contact point of view) is positive. The boundary conditions give a system of four equations with four unknowns from which the constants a,b,c,d are extracted. Using $\sigma = 1/R_{sq}$, we find the expression for $R_{nl}(L)$, given by Eq. (3).

An alternative and more intuitive explanation of the conductivity mismatch problem taking place at both the injector and detector is as follows. A large spin accumulation in graphene implies a large splitting of the electrochemical potentials for the two spin channels which cannot develop if the channels are shorted by the low impedance of the injector and detector electrodes. This is not the case of 100% spin-polarized electrodes since the two spin channels in graphene are not connected to each other by the injector and detector electrodes.

In the presence of an external magnetic field applied in the z direction the general solutions of the spin-up electrochemical potential are of the form[32]

$$\begin{pmatrix}\mu_{\uparrow x}\\ \mu_{\uparrow y}\\ \mu_{\uparrow z}\end{pmatrix}^{0,L} = A_{\mp}^{0,L}\begin{pmatrix}0\\0\\1\end{pmatrix}\exp(\pm K_1 x) + B_{\mp}^{0,L}\begin{pmatrix}1\\-i\\0\end{pmatrix}\exp(\pm K_2^{-}x) + C_{\mp}^{0,L}\begin{pmatrix}1\\i\\0\end{pmatrix}\exp(\pm K_2^{+}x), \tag{A4}$$

where the $-$ $(+)$ sign corresponds to the positive (negative) x direction and K_1 and $K_2^{\pm}$ are given by $K_1 = (\sqrt{D\tau})^{-1} = \lambda^{-1}$ and $K_2^{\pm} = \lambda^{-1}\sqrt{1 \pm i\omega\tau}$. Since the electrochemical potential cannot increase when x approaches $-(+)\infty$, the solutions for $x<0$ $(x>L)$ contain only the exponentially decaying terms, i.e., the terms containing $+K_{1,2}$ for $x<0$ and the terms $-K_{1,2}$ for $x>L$. For $0<x<L$ the solutions contain six terms so that the back flow of spins due to the presence of the detector is taken into account. There are in total twelve coefficients $(A_+^0, B_+^0, C_+^0, A_-^0, B_-^0, C_-^0, A_+^L, B_+^L, C_+^L, A_-^L, B_-^L, C_-^L)$ that describe the solutions. These are found from the boundary conditions: the continuity of electrochemical potentials and the spin current conservation laws which we apply for each of x, y, and z components. The continuity of the electrochemical potentials give in total six equations: three for injection and three for detection. The spin current conservation laws give another six equations and they are written in a similar manner as it was described above. Except the x component $I_x(0)$ all the other spin current components $I_y(0), I_z(0), I_x(L), I_y(L), I_z(L)$ are null. The spin-up electrochemical potential present at the detector (x component) is given by

$$\mu_{\uparrow}(L) = B_-^L\exp(-K_2^{-}L) + C_-^L\exp(-K_2^{+}L). \tag{A5}$$

The boundary conditions give a system of twelve equations with twelve unknowns. For given τ and D we solve the system of equations numerically to find the coefficients B_-^L and C_-^L for each value of the magnetic field. P is just a multiplication factor. We calculate a series of precession curves for a mesh given by different values of τ and D. From this set of curves we choose the one that shows the smallest deviation from the experiment by the least-mean-squares method. The parameters τ, D, P corresponding to this curve represent the best fit.

*Present address: II. Physikalisches Institut A, RWTH Aachen University, Germany; popinciuc@physik.rwth-aachen.de

[1] W. J. M. Naber, S. Faez, and W. G. van der Wiel, J. Phys. D: Appl. Phys. **40**, R205 (2007).
[2] E. W. Hill, A. K. Geim, K. Novoselov, F. Schedin, and P. Blake, IEEE Trans. Magn. **42**, 2694 (2006).
[3] N. Tombros, C. Jozsa, M. Popinciuc, H. T. Jonkman, and B. J. van Wees, Nature (London) **448**, 571 (2007).
[4] S. Cho, Y.-F. Chen, and M. S. Fuhrer, Appl. Phys. Lett. **91**, 123105 (2007).
[5] M. Nishioka and A. M. Goldman, Appl. Phys. Lett. **90**, 252505 (2007).
[6] M. Ohishi, M. Shiraishi, R. Nouchi, T. Nozaki, T. Shinjo, and Y. Suzuki, Jpn. J. Appl. Phys. **46**, L605 (2007).
[7] W. H. Wang, K. Pi, Y. Li, Y. F. Chiang, P. Wei, J. Shi, and R. K. Kawakami, Phys. Rev. B **77**, 020402(R) (2008).
[8] N. Tombros, S. Tanabe, A. Veligura, C. Jozsa, M. Popinciuc, H. T. Jonkman, and B. J. van Wees, Phys. Rev. Lett. **101**, 046601 (2008).
[9] C. Jozsa, M. Popinciuc, N. Tombros, H. T. Jonkman, and B. J. van Wees, Phys. Rev. Lett. **100**, 236603 (2008).
[10] H. Goto, A. Kanda, T. Sato, S. Tanaka, Y. Ootuka, S. Odaka, H. Miyazaki, K. Tsukagoshi, and Y. Aoyagi, Appl. Phys. Lett. **92**, 212110 (2008).
[11] C. Jozsa, M. Popinciuc, N. Tombros, H. T. Jonkman, and B. J. van Wees, Phys. Rev. B **79**, 081402(R) (2009).
[12] M. Shiraishi, M. Ohishi, R. Nouchi, T. Nozaki, T. Shinjo, and Y. Suzuki, Adv. Funct. Mater. **19**, 3711 (2009).
[13] W. Han, W. H. Wang, K. Pi, K. M. McCreary, W. Bao, Y. Li, F. Miao, C. N. Lau, and R. K. Kawakami, Phys. Rev. Lett. **102**, 137205 (2009).
[14] W. Han, K. Pi, W. Bao, K. M. McCreary, Y. Li, W. H. Wang, C. N. Lau, and R. K. Kawakami, Appl. Phys. Lett. **94**, 222109 (2009).
[15] K. S. Novoselov, A. K. Geim, S. V. Morozov, D. Jiang, Y. Zhang, S. V. Dubonos, I. V. Grigorieva, and A. A. Firsov, Science **306**, 666 (2004).
[16] A. K. Geim and K. S. Novoselov, Nature Mater. **6**, 183 (2007).
[17] K. I. Bolotin, K. J. Sikes, Z. Jiang, M. Klima, G. Fudenberg, J. Hone, P. Kim, and H. L. Stormer, Solid State Commun. **146**, 351 (2008).
[18] C. L. Kane and E. J. Mele, Phys. Rev. Lett. **95**, 226801 (2005).
[19] D. Huertas-Hernando, F. Guinea, and A. Brataas, Phys. Rev. B **74**, 155426 (2006).
[20] H. Min, J. E. Hill, N. A. Sinitsyn, B. R. Sahu, L. Kleinman, and A. H. MacDonald, Phys. Rev. B **74**, 165310 (2006).
[21] Y. Yao, F. Ye, X.-L. Qi, S.-C. Zhang, and Z. Fang, Phys. Rev. B **75**, 041401(R) (2007).
[22] D. Huertas-Hernando, F. Guinea, and A. Brataas, Phys. Rev. Lett. **103**, 146801 (2009).
[23] M. Gmitra, S. Konschuh, C. Ertler, C. Ambrosch-Draxl, and J. Fabian, arXiv:0904.3315 (unpublished).
[24] C. Ertler, S. Konschuh, M. Gmitra, and J. Fabian, Phys. Rev. B **80**, 041405 (2009).
[25] A. H. Castro Neto and F. Guinea, Phys. Rev. Lett. **103**, 026804 (2009).
[26] G. Schmidt, D. Ferrand, L. W. Molenkamp, A. T. Filip, and B. J. van Wees, Phys. Rev. B **62**, R4790 (2000).
[27] E. I. Rashba, Phys. Rev. B **62**, R16267 (2000).
[28] A. Fert and H. Jaffres, Phys. Rev. B **64**, 184420 (2001).
[29] D. L. Smith and R. N. Silver, Phys. Rev. B **64**, 045323 (2001).
[30] S. Takahashi and S. Maekawa, Phys. Rev. B **67**, 052409 (2003).
[31] A. van Staa, J. Wulfhorst, A. Vogel, U. Merkt, and G. Meier, Phys. Rev. B **77**, 214416 (2008).
[32] N. Tombros, Ph.D. thesis, University of Groningen, The Netherlands, 2008, http://irs.ub.rug.nl/ppn/310621852
[33] B. J. Jönsson-Åkerman, R. Escudero, C. Leighton, S. Kim, I. K. Schuller, and D. A. Rabson, Appl. Phys. Lett. **77**, 1870 (2000).
[34] M. Johnson and R. H. Silsbee, Phys. Rev. B **37**, 5312 (1988).
[35] F. J. Jedema, H. B. Heersche, A. T. Filip, J. J. A. Baselmans, and B. J. van Wees, Nature (London) **416**, 713 (2002).
[36] P. C. van Son, H. van Kempen, and P. Wyder, Phys. Rev. Lett. **58**, 2271 (1987).
[37] J. Fabian, A. Matos-Abiague, C. Ertler, P. Stano, and I. Žutić, Acta Phys. Slov. **57**, 565 (2007).
[38] T. Kimura and Y. Otani, Phys. Rev. Lett. **99**, 196604 (2007).
[39] C. Jozsa, T. Maassen, M. Popinciuc, P. Zomer, A. Veligura, H. Jonkman, and B. van Wees, Phys. Rev. B **80**, 241403(R) (2009).
[40] P. G. Elliott, Phys. Rev. **96**, 266 (1954).
[41] Y. Yafet, in *Solid State Physics*, edited by F. Seitz and D. Turnbull (Academic, New York, 1963), Vol. 13.
[42] M. I. D'yakonov and V. I. Perel', Sov. Phys. Solid State **13**, 3023 (1972).
[43] M. I. D'yakonov and V. Y. Kachorovskii, Sov. Phys. Semicond. **20**, 110 (1986).
[44] F. J. Jedema, M. V. Costache, H. B. Heersche, J. J. A. Baselmans, and B. J. van Wees, Appl. Phys. Lett. **81**, 5162 (2002).